MIT Open Access Articles

Polarization fields: dynamic light field display using multi-layer LCDs

Citation: Douglas Lanman, Gordon Wetzstein, Matthew Hirsch, Wolfgang Heidrich, and Ramesh Raskar. 2011. Polarization fields: dynamic light field display using multi-layer LCDs. In Proceedings of the 2011 SIGGRAPH Asia Conference (SA '11). ACM, New York, NY, USA, Article 186, 10 pages.

As Published: http://dx.doi.org/10.1145/2024156.2024220

Publisher: Association for Computing Machinery (ACM)

Persistent URL: http://hdl.handle.net/1721.1/80393

Version: Author's final manuscript: final author's manuscript post peer review, without publisher's formatting or copy editing

Massachusetts Institute of Technology

Polarization Fields: Dynamic Light Field Display using Multi-Layer LCDs

Douglas Lanman[1]   Gordon Wetzstein[2]   Matthew Hirsch[1]   Wolfgang Heidrich[2]   Ramesh Raskar[1]

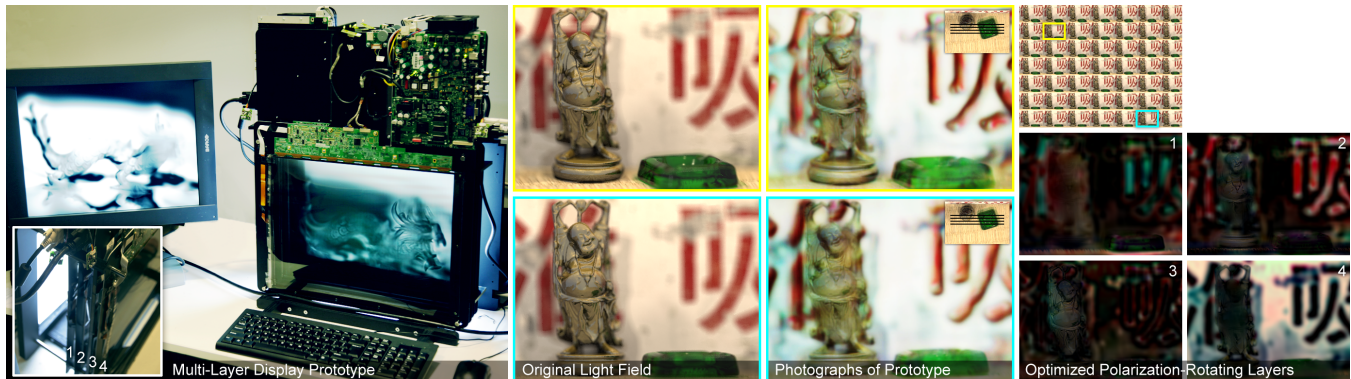[1]MIT Media Lab   [2]University of British Columbia

Figure 1: *Dynamic light field display using polarization field synthesis with multi-layered LCDs. (Left) We construct an optically-efficient polarization field display by covering a stack of liquid crystal panels with crossed linear polarizers. Each layer functions as a polarization rotator, rather than as a conventional optical attenuator. (Right, Top) A target light field. (Right, Bottom) Light fields are displayed, at interactive refresh rates, by tomographically solving for the optimal rotations to be applied at each layer. (Middle) A pair of simulated views is compared to corresponding photographs of the prototype on the left and right, respectively. Inset regions denote the relative position with respect to the display layers, shown as black lines, demonstrating objects can extend beyond the display surface.*

Abstract

We introduce polarization field displays as an optically-efficient design for dynamic light field display using multi-layered LCDs. Such displays consist of a stacked set of liquid crystal panels with a single pair of crossed linear polarizers. Each layer is modeled as a spatially-controllable polarization rotator, as opposed to a conventional spatial light modulator that directly attenuates light. Color display is achieved using field sequential color illumination with monochromatic LCDs, mitigating severe attenuation and moiré occurring with layered color filter arrays. We demonstrate such displays can be controlled, at interactive refresh rates, by adopting the SART algorithm to tomographically solve for the optimal spatially-varying polarization state rotations applied by each layer. We validate our design by constructing a prototype using modified off-the-shelf panels. We demonstrate interactive display using a GPU-based SART implementation supporting both polarization-based and attenuation-based architectures. Experiments characterize the accuracy of our image formation model, verifying polarization field displays achieve increased brightness, higher resolution, and extended depth of field, as compared to existing automultiscopic display methods for dual-layer and multi-layer LCDs.

Keywords: computational displays, light fields, automultiscopic 3D displays, tomography, multi-layer LCDs

Links: ◆DL ⯐PDF ⊕WEB ▶VIDEO ▨DATA ⬆CODE

1 Introduction

The emergence of consumer, glasses-based stereoscopic displays has renewed interest in glasses-free automultiscopic alternatives. Manufacturers are beginning to offer such displays, primarily using two technologies: parallax barriers [Ives 1903] and integral imaging [Lippmann 1908]. These approaches have well-documented limitations compared to stereoscopic displays: decreased resolution, potentially reduced brightness, and narrow depths of field (objects separated from the display appear blurred). Alternatives are being pursued, spanning volumetric to holographic systems; yet, particularly for mobile devices, a display is required that leverages existing or emerging spatial light modulation technologies compatible with thin form factors and having minimal power consumption.

We are inspired by systems that address these issues using well-developed LCD technology. Jacobs et al. [2003] demonstrate dual-layer LCDs can be operated as parallax barriers, allowing full-resolution 2D content and 3D modes with reduced resolution and brightness. Lanman et al. [2010] increase the optical efficiency of dual-layer LCDs with content-adaptive parallax barriers, although at the cost of increased computation. Several researchers have considered automultiscopic multi-layer LCDs. Loukianitsa and Putilin [2002; 2006] evaluate three-layer designs. More recently, Gotoda [2010] and Wetzstein et al. [2011] propose tomographically-optimized multi-layer LCDs. Yet, these works share a common architecture: LCDs are stacked such that each layer implements a spatial light modulator that *attenuates* light.

This paper introduces optically-efficient architectures and computationally-efficient algorithms for automultiscopic display using multi-layered LCDs. In contrast to prior work, we operate these layered architectures as *polarization field displays*: constructed by covering multiple liquid crystal panels with a single pair of crossed linear polarizers. Each layer, if properly designed, functions as a *polarization rotator*, rather than as a light attenuator. We propose an efficient tomographic solver, specially-suited to this design, that enables interactive applications. Through polarization field displays we endeavor to leverage existing and emerging LCD technology for practical dynamic light field display.

1.1 Contributions

We optimize the optical and computational efficiency of multi-layer LCDs for dynamic light field display. Our contributions include:

- We introduce polarization field displays to achieve increased brightness, higher resolution, and extended depth of field, compared to existing dual-layer and multi-layer LCDs.
- We cast polarization-based light field display as a constrained linear least-squares problem and demonstrate the simultaneous algebraic reconstruction technique (SART) allows dynamic light field display for both polarization-based and attenuation-based multi-layer LCD architectures.
- We implement a prototype multi-layer LCD using modified off-the-shelf panels and demonstrate interactive display using a GPU-based SART solver. This prototype confirms the optical efficiency of our design employing field sequential color, a pair of crossed polarizers, and layered, monochromatic LCDs.

1.2 Overview of Benefits and Limitations

As shown in Figure 2, we construct a polarization field display and compare its performance to an attenuation-based design. While inspired by Gotoda [2010; 2011] and Wetzstein et al. [2011], our construction is the first to extend the benefits established in those works to dynamic imagery. Our construction offers similar benefits in resolution, brightness, and depth of field, while exhibiting fewer artifacts. We further optimize brightness by eliminating unnecessary polarizing films and color filter arrays. While prior attenuation-based displays were optimized off-line, our GPU-based SART solver is the first to enable control of either attenuation-based or polarization-based displays at interactive refresh rates.

Our design shares the limitations of other multi-layer LCDs, including added thickness, complexity, and cost. Layered constructions attenuate light and cause moiré. Field sequential color reduces attenuation, but requires high-speed monochromatic panels and strobed backlighting. While Bell et al. [2008] mitigate moiré with diffusers, we do not use such elements. Unlike the periodic viewing zones of parallax barriers and integral imaging [Dodgson 2009], our design reproduces only the central zone and tracking is necessary for wider fields of view. We require control of the polarization properties of LCDs, since panels are assumed to operate as polarization rotators. Off-the-shelf LCDs deviate from this model, particularly for oblique viewing or due to multiple liquid crystal domains [Yeh and Gu 2009]. Commercial embodiments will require models with increased fidelity, possibly complicating real-time control, or engineering of panels with the desired optical properties.

2 Related Work

2.1 Layered Automultiscopic Displays

Automultiscopic displays present multi-view imagery to one or more users without special eyewear. Practical methods supporting dynamic imagery include volumetric displays using either a single, mechanically-rotated spatial light modulator [Favalora 2005] or layered, static constructions. The latter category includes additive combinations of emissive displays, typically achieved with beam-splitters [Akeley et al. 2004], semi-transparent displays [Sullivan 2003], or passive optical scatters [Nayar and Anand 2007]. Layered combinations of attenuating layers have been considered by Loukianitsa and Putilin [2002; 2006] and Gotoda [2010]. We note iZ3D commercialized a dual-layer stereoscopic LCD that used a single polarization-rotating layer, although viewers were required to wear polarized glasses. In closely-related works, Gotoda [2011]
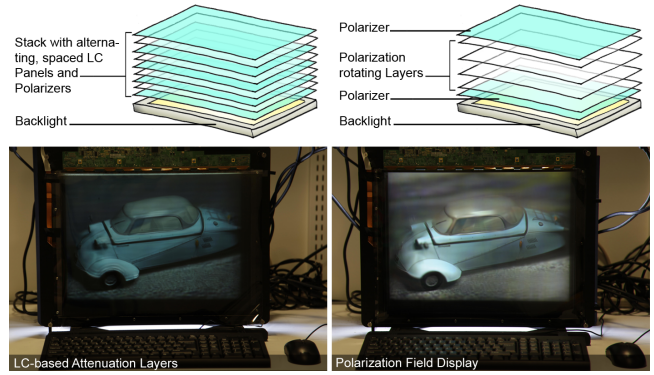

Figure 2: *Polarization-based vs. attenuation-based multi-layer LCDs. (Top, Left) An attenuation-based light field display requires stacking liquid crystal panels with polarizers between each layer. This construction effectively creates a programmable transparency stack. (Top, Right) Polarization-based light field displays improve optical efficiency using a single pair of crossed polarizers. (Bottom) Corresponding photographs of the prototype configured as a an attenuation-based vs. polarization-based multi-layer LCD.*

proposes optimizing the polarization properties of layered LCDs and Wetzstein et al. [2011] extend tomographic optimization principles to multi-layered, attenuation-based displays. Our contributions, relative to these works, include: introducing a unifying image formation model and real-time tomographic optimization for both attenuation-based and polarization-based light field displays, proposing optically-efficient polarization field displays using layered polarization rotators, and analyzing the performance of a working prototype supporting interactive refresh rates.

2.2 Liquid Crystal Displays

Constructing polarization field displays requires an accurate characterization of the optical properties of LCDs. The transformation of polarized light due to passage through layered materials is modeled by the Jones calculus [Jones 1941]. Orthogonal components of the electric field are represented as a complex-valued Jones vector. The optical action of a given element (e.g., a birefringent layer or polarizing film) is represented by a Jones matrix, with the product of this matrix and a Jones vector encoding the polarization state transformation. Yeh and Gu [2009] formally characterize the polarization properties of LCDs, providing analytic Jones matrices for common technologies, including twisted nematic (TN), vertical alignment (VA), and in-plane switching (IPS) panels. In this paper we consider a unifying, but simplified, Jones matrix model, wherein LCDs are approximated as spatially-controllable polarization rotators.

Applying a more detailed Jones matrix model for our modified off-the-shelf panels has the potential to reduce visible artifacts in the prototype, possibly at the cost of decreased refresh rates due to increased computational complexity (see Appendix A). Moreno et al. [2003] estimate the Jones matrix of an LCD using seven irradiance measurements, two linear polarizers, and a single quarter-wave plate. Ma et al. [2010] propose a simplified calibration using only three measurements. A promising alternative to these model-based refinements is to directly engineer LCD panels to act as polarization rotators. Davis et al. [2000] implement such panels using a custom parallel-aligned LCD covered by a pair of crossed quarter-wave plates. Moreno et al. [2007] construct a polarization rotator using a conventional TN panel. In both works, the liquid crystal is operated as a voltage-controlled wave plate to produce polarization state rotations. Layered constructions of such panels are ideally suited to implement practical polarization field displays.

3 Polarization Field Displays

This section describes how to optimally construct polarization field displays to emit a target light field using multi-layer LCDs. First, we review conventional, single-layer LCD components and operation principles. Second, a general image formation model is described for polarization field displays, encompassing multi-layer LCDs as one embodiment. Under this model, each liquid crystal panel is considered as a spatially-controllable polarization rotator, and the entire set of panels is enclosed by a single pair of crossed linear polarizers. Third, we describe how to display dynamic light fields using polarization fields by adapting real-time tomographic algorithms to satisfy a least-squares optimality criterion.

3.1 Overview of LCDs

A liquid crystal display (LCD) contains two primary components: a backlight and a spatial light modulator (SLM). The backlight is designed to produce uniform illumination, typically by conditioning the light produced by a cold cathode fluorescent lamp (CCFL) or a light-emitting diode (LED) array, using a light guide and various diffusing and brightness-enhancing films. The spatial light modulator is a thin layer of liquid crystal, enclosed between glass sheets with embedded, two-dimensional electrode arrays. This stack is further enclosed by a pair of crossed linear polarizers.

Applying a voltage across an electrode pair alters the polarization properties of a pixel. We assume the effect can be approximated as inducing a rotation of the polarization state of light rays traversing the pixel. This holds to varying degrees of accuracy for off-the-shelf LCDs (see Appendix A and Supplementary Appendix C). Yet, following Davis et al. [2000] and Moreno et al. [2007], such polarization rotators can be constructed by modifying existing LCDs. Under this model the transmitted intensity I is given by Malus' law:

$$I = I_0 \sin^2(\theta), \qquad (1)$$

where I_0 is the intensity after passing through the first polarizer and θ is the angle of polarization after passing through the liquid crystal, defined relative to the axis of the first polarizer [Hecht 2001]. By controlling the voltages applied across the electrode array, two-dimensional images are rendered with varying shades of gray depending on the induced rotation. The rotation angle θ must vary only over the interval $[0, \pi/2]$ radians to reproduce all shades of gray—the range afforded by most commercial LCD panels, including widespread twisted nematic (TN) architectures. We note that this model only strictly applies for rays oriented perpendicular to the display surface. At oblique angles, light leakage occurs through crossed polarizers and birefringence of the liquid crystal produces elliptical, rather than linear, polarization states [Yeh and Gu 2009]. However, as experimentally verified in Section 4, this model is sufficient for the viewing angles considered in the prototype.

Two design alternatives enable color LCDs: color filter arrays and field sequential color. In current LCDs, a color filter array is deposited on the glass sheet closest to the viewer. Each pixel is divided into three subpixels by an array of filters with spectral transmittances corresponding to three color primaries. This requires the resolution to be tripled along one display axis, increasing fabrication complexity and cost. Color filter arrays also decrease brightness, typically to 30% of the backlight intensity. Rather than brightening the backlight, which reduces power efficiency, field sequential color (FSC) can be employed. With FSC, a strobed backlight successively illuminates a high-speed monochromatic LCD with varying color sources. If strobing occurs faster than the human flicker fusion threshold [Hart 1987], a color image is perceived. While yet to be widely commercially available, FSC LCDs are an active area of research [Stewart and Roach 1994; Chen et al. 2009].

3.2 Modeling Multi-Layer LCDs

In this section we consider how multi-layer LCDs can be constructed to emit a four-dimensional light field, rather than a two-dimensional image. As shown in Figure 2, we consider the following architecture: a backlight covered by multiple, disjoint spatial light modulators. First, to maximize the optical efficiency, we assume field sequential color illumination; this eliminates K layers of color filters that would otherwise cause severe moiré [Bell et al. 2008] and brightness attenuation by a factor of approximately 0.3^K (e.g., 2.7% transmission for a three-layer LCD). Second, we observe that only two polarizing films are necessary, one on the top and bottom of the multi-layer stack. This creates a *polarization field display*, wherein each spatial light modulator consists of a liquid crystal layer functioning as a spatially-addressable, voltage-controlled polarization rotator.

Such displays must be controlled so the polarization field incident on the last polarizer accurately reproduces the target light field. In this section we present our analysis in flatland, considering 1D layers and 2D light fields, with a direct extension to 2D layers and 4D light fields. As shown in Figure 3, we consider a display of width w and height h, with K layers distributed along the y-axis such that $d_k \in [-h/2, h/2]$. A two-plane light field parameterization $l(u, a)$ is used [Chai et al. 2000]. The u-axis is coincident with the x-axis and the slope of ray (u, a) is defined as $a = s - u = d_r \tan(\alpha)$, where the s-axis is a distance d_r from the u-axis.

The emitted light field $l(u, a)$ is given by applying Equation 1 to the polarization field $\theta(u, a)$ incident on the front polarizer:

$$l(u, a) = l_0(u, a) \sin^2(\theta(u, a)), \qquad (2)$$

where $l_0(u, a)$ is the light field produced by the backlight after attenuation by the rear polarizer. The backlight is assumed to be uniform such that $l_0(u, a) = l_{max}$ and the light field is normalized such that $l(u, a) \in [0, l_{max}]$. This expression is used to solve for the necessary target polarization field $\theta(u, a)$, as follows.

$$\theta(u, a) = \pm \sin^{-1} \left(\sqrt{\frac{l(u, a)}{l_0(u, a)}} \right) \bmod \pi \qquad (3)$$

Under these assumptions, the principal value of the arcsine ranges over $[0, \pi/2]$. Note, with full generality, the target polarization field is multi-valued and periodic, since a rotation of $\pm\theta \bmod \pi$ radians will produce an identical intensity by application of Malus' law.
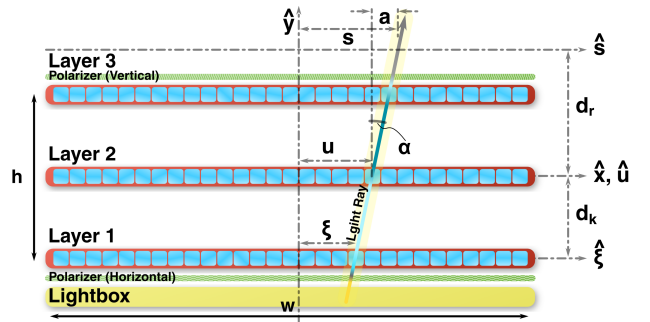

Figure 3: *Polarization field displays. A K-layer display is constructed by separating multiple liquid crystal panels. The light field $l_0(u, a)$ emitted by the backlight is linearly polarized by the rear polarizer. The polarization state of ray (u, a) is rotated by $\phi_k(\xi)$ after passage through layer k, where $\xi = u + (d_k/d_r)a$. The emitted light field $\tilde{l}(u, a)$ is given by applying Equation 2 to the emitted polarization field $\tilde{\theta}(u, a)$ upon passage through the front polarizer.*

Figure 4: *GPU-based SART allows real-time multi-layer optimization approaching the fidelity of the off-line solver. The first and second columns show different target views. Polarization-rotating layers are shown below each example. The off-line reference solver [Coleman and Li 1996] produces sharp reconstructions (second row). A small number of SART iterations causes blurring (third row). Additional iterations converge to the reference (bottom row), with five iterations yielding similar quality (fourth row). Note that simulated views are shown, rather than prototype results.*

Each layer controls the spatially-varying polarization state rotation $\phi_k(\xi)$, as induced at point ξ along layer k. Ray (u, a) intersects the K layers, accumulating incremental rotations at each intersection, such that the emitted polarization field $\tilde{\theta}(u, a)$ is given by

$$\tilde{\theta}(u, a) = \sum_{k=1}^{K} \phi_k(u + (d_k/d_r)a). \quad (4)$$

Combining Equations 2 and 4 yields the following model for the light field $\tilde{l}(u, a)$ emitted by a K-layer polarization field display:

$$\tilde{l}(u, a) = l_0(u, a) \sin^2 \left(\sum_{k=1}^{K} \phi_k(u + (d_k/d_r)a) \right). \quad (5)$$

3.3 Synthesizing Polarization Fields

This section describes the optimization of multi-layer LCDs for polarization field display. We consider a discrete parameterization for which the emitted polarization field is represented as a column vector $\tilde{\theta}$ with M elements, each of which corresponds to the angle of polarization for a specific light field ray. Similarly, the polarization state rotations are represented as a column vector ϕ with N elements, each of which corresponds to a specific display pixel in a given layer. Under this parameterization, Equation 4 yields a linear model such that

$$\tilde{\theta}_m = \sum_{n=1}^{N} P_{mn} \phi_n, \quad (6)$$

where $\tilde{\theta}_m$ and ϕ_n denote ray m and pixel n of $\tilde{\theta}$ and ϕ, respectively. An element P_{mn} of the projection matrix $\mathbf{P}$ is given by the normalized area of overlap between pixel n and ray m, occupying a finite region determined by the sample spacing.

An optimal set of polarization state rotations ϕ is found by solving the following constrained linear least-squares problem:

$$\arg\min_{\phi} \|\theta - \mathbf{P}\phi\|^2, \text{ for } \phi_{min} \leq \phi \leq \phi_{max}, \quad (7)$$

where each layer can apply a rotation ranging over $[\phi_{min}, \phi_{max}]$. Similar to Wetzstein et al. [2011], Equation 7 can be solved using a sparse, constrained, large-scale trust region method [Coleman and Li 1996]. However, we observe that this problem can be solved more efficiently by adapting the simultaneous algebraic reconstruction technique (SART). As proposed by Andersen and Kak [1984] and further described by Kak and Slaney [2001], SART provides an iterative solution wherein the estimate $\phi^{(q)}$ at iteration q is given by

$$\phi^{(q)} = \phi^{(q-1)} + \mathbf{v} \circ (\mathbf{P}^\top (\mathbf{w} \circ (\theta - \mathbf{P}\phi^{(q-1)}))), \quad (8)$$

where $\circ$ denotes the Hadamard product for element-wise multiplication and elements of the $\mathbf{w}$ and $\mathbf{v}$ vectors are given by

$$w_m = \frac{1}{\sum_{n=1}^{N} P_{mn}} \quad \text{and} \quad v_n = \frac{1}{\sum_{m=1}^{M} P_{mn}}. \quad (9)$$

After each iteration, additional constraints on $\phi^{(q)}$ are enforced by clamping the result to the feasible rotation range. Building upon the Kaczmarz method for solving linear systems of equations [Kaczmarz 1937], SART is shown to rapidly converge to a solution approaching the fidelity of that produced by alternative iterative methods, including trust region and conjugate gradient descent techniques [Kak and Slaney 2001] (see Figure 4). In Section 4 we show that SART allows for real-time optimization for interactive polarization field displays.

In summary, polarization fields present both an optically and computationally efficient architecture for dynamic light field display using multi-layer LCDs. We briefly contrast this architecture to that required for a direct extension of the attenuation-based method proposed by Wetzstein et al. [2011]. As shown in Figure 2, a multi-layered, attenuation-based display is fabricated by placing a polarizer on the backlight and additional polarizers after each liquid crystal layer, effectively creating a set of dynamically-programmable transparencies; however, such a design reduces the display brightness by a factor of 0.8^{K-2} compared to the proposed polarization field display, assuming a maximal transmission of 80% through each polarizer (as measured for those used in the prototype). Yet, we observe our adaptation of SART can similarly be applied to attenuation layers by substituting the logarithm of the emitted light field intensity $\tilde{l}_m$ and the logarithm of the transmittance t_n for $\tilde{\theta}_m$ and ϕ_n in Equation 6, respectively; thus, we provide the first implementation for achieving interactive frame rates with such designs.
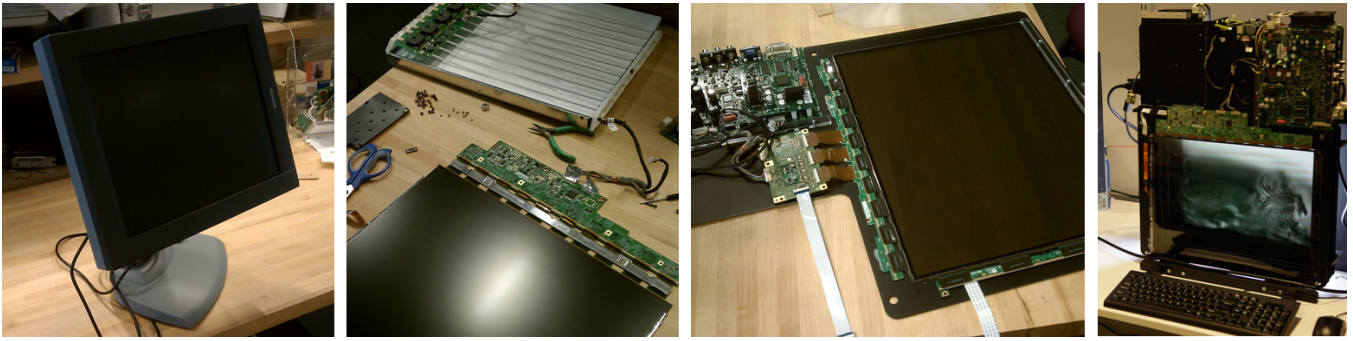
Figure 5: *Constructing the polarization field display prototype. Four monochromatic LCDs were modified to create a single multi-layer LCD. Photographs depict from left to right: an unmodified Barco E-2320 PA LCD, the liquid crystal panel and backlight after removing the case and power supply, a modified panel mounted on an aluminum frame, and the assembled prototype.*

4 Implementation and Assessment

This section describes the construction and performance of the prototype. First, we summarize the modifications made to commercial LCD panels to create a reconfigurable multi-layer display. Second, we review the off-line and real-time software for light field rendering, antialiasing, and optimizing layer patterns. Third, we assess the prototype, evaluating our image formation model and illustrating the practical benefits and limitations of polarization field displays.

4.1 Implementation

4.1.1 Hardware

Given that we require monochromatic layers and field sequential color, a custom prototype was necessary. PureDepth [Bell et al. 2008] offers dual-layer LCDs, but no supplier was found for multi-layer configurations. Each layer of the prototype consists of a modified Barco E-2320 PA LCD, supporting 1600×1200 8-bit grayscale display at 60 Hz, and an active area of 40.8×30.6 cm. As shown in Figure 5, the liquid crystal layer was separated from the case, backlight, and power supply. Polarizing films were removed and the adhesive was dissolved with acetone. By design, the driver board is folded behind the panel, blocking a portion of the display when used in a stacked configuration. An extended ribbon cable was constructed to allow the board to be folded above the display using a pair of 20-pin connectors and a flat flexible cable. The exposed panel, driver boards, and power supply were mounted to a waterjet-cut aluminum frame. Four such panels were constructed and stacked on a wooden stand. Arbitrary layer spacings are supported by translating the frames along rails. Acrylic spacers hold the layers at a fixed spacing of 1.7 cm for all experiments described in this paper, yielding a total display thickness of 5.1 cm. The prototype is illuminated using an interleaved pair of backlights and controlled by a 3.4 GHz Intel Core i7 workstation with 4 GB of RAM. A four-head NVIDIA Quadro NVS 450 graphics card synchronizes the displays. See Appendix A for additional discussion of the prototype, as well as Supplementary Appendices A and C.

As shown in Figure 2, the display operates in either attenuation-based or polarization-based modes. The original polarizers were discarded and replaced with American Polarizers AP38-006T linear polarizers. By specification, a single polarizer has a transmission efficiency of 38% for unpolarized illumination. Transmission is reduced to 30% through a pair of aligned polarizers, yielding an efficiency of 80% for polarized light passing through a single, aligned polarizer. Five polarizers are required for attenuation-based display, with a pair of crossed polarizers on the rear layer followed by successively-crossed polarizers on each remaining layer. A po-
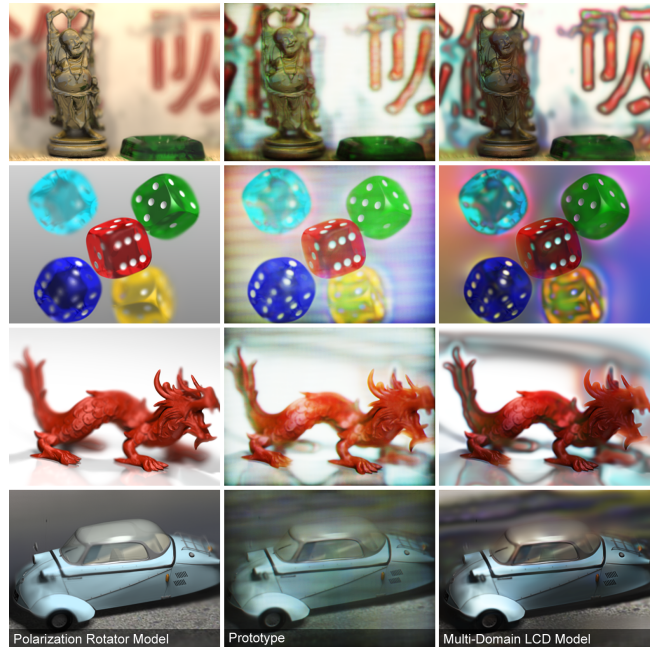

Figure 6: *Polarization field display using the multi-layer prototype. The central views for the "Buddha", "dice", "dragon", and "car" scenes are shown. Views predicted by the polarization rotator model (Equation 5) and the multi-domain LCD model (Equation 15) are compared in the left and right columns, respectively. Photographs of the prototype are shown in the middle. Section 4.2 and Appendix A quantitatively assess performance and artifacts.*

larization field display is implemented by enclosing the stack by a single pair of crossed polarizers. Field sequential color is simulated, for still imagery, by combining three photographs taken while alternating the color channel displayed on each layer. To assist registration, examples in this paper use the color filters included in the Bayer mosaic of the camera, whereas the video summarizes experiments using Roscolux filters (#26, #91, and #80) placed on the backlight. The video shows dynamic examples in grayscale.

Each panel must be radiometrically calibrated to allow an accurate mapping from optimized rotation angles to displayed image values. The Barco E-2320 PA is intended for medical diagnostic imaging and replicates the DICOM Grayscale Standard Display Function. The normalized displayed intensity $I \in [0, 1]$ was measured as a function of the 8-bit image value $v \in [0, 255]$ using a photometer held against an unmodified panel. The resulting radiometric
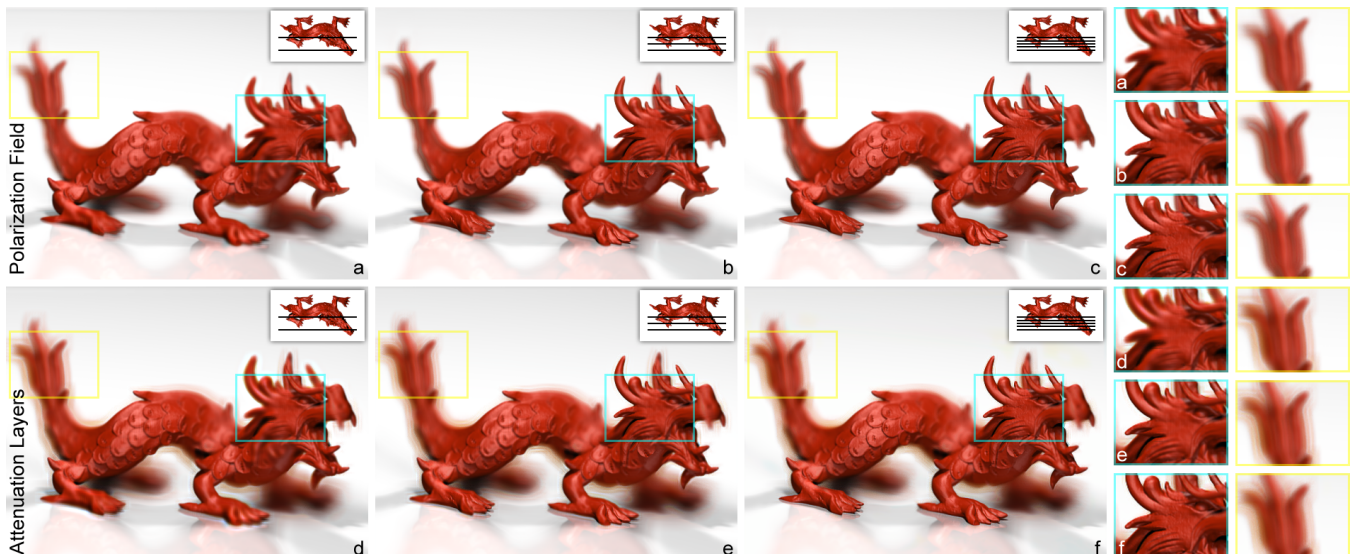
Figure 7: *Simulated light field reconstructions using polarization fields (top row) and attenuation layers (bottom row) are shown for two, three, and five layers from left to right. Layer positions with respect to the scene are illustrated in the insets. Note that the reconstruction fidelity of objects within and outside the physical display extent increases for a larger number of layers, as highlighted by the cyan and yellow regions, respectively. Due to bias in the least-squares solution for a log-domain objective, optimized tomographic reconstructions for attenuation-based displays suffer from halo artifacts around high-contrast edges, which is not the case for polarization field displays.*

response curve is approximated by a gamma value of $\gamma = 3.5$ such that $I = (v/255)^\gamma$. Thus, gamma compression maps optimized pixel transmittances to image values when operating in the attenuation-based mode. When operated as a polarization field display, optimization yields the polarization state rotation ϕ for each pixel. For an unmodified panel we model this mapping by Equation 1 such that $I = \sin^2(\phi)$. Equating this with the gamma curve yields the following mapping between rotations and image values.

$$v(\phi) = \lfloor 255 \sin^{2/\gamma}(\phi) + 0.5 \rfloor \tag{10}$$

Figures 1 and 6 compare modeled light field views to corresponding photographs of the prototype. Figure 2 compares the attenuation-based mode to the polarization-based mode.

4.1.2 Software

The light fields in this paper are rendered with a spatial resolution of 512×384 pixels and depict 3D scenes with both horizontal and vertical parallax from 7×7 viewpoints within a field of view of 10 degrees. POV-Ray is used to render the scenes shown in Figure 6. Following Levoy and Hanrahan [1996] and Zwicker et al. [2006], we apply a 4D antialiasing filter to the light fields by rendering each view with a limited depth of field. As analyzed by Wetzstein et al. [2011], this antialiasing filter simultaneously approximates the limited depth of field established for multi-layer light field displays.

The Matlab LSQLIN solver serves as the reference solution to Equation 7, implementing a sparse, constrained, large-scale trust region method [Coleman and Li 1996]. This solver converges in about 8 to 14 iterations for three to five attenuating or polarization-rotating layers. Solutions are found within approximately 10 minutes on the previously-described Intel Core i7 workstation.

The SART algorithm given by Equation 8 is implemented in Matlab and on the GPU. We observe SART is well-suited for parallel processing on programmable GPUs [Keck et al. 2009]. Our code is programmed in C++, OpenGL, and Cg. Light fields are rendered and antialiased in real-time using OpenGL, followed by several iterations of the GPU-based SART implementation. We achieve re-
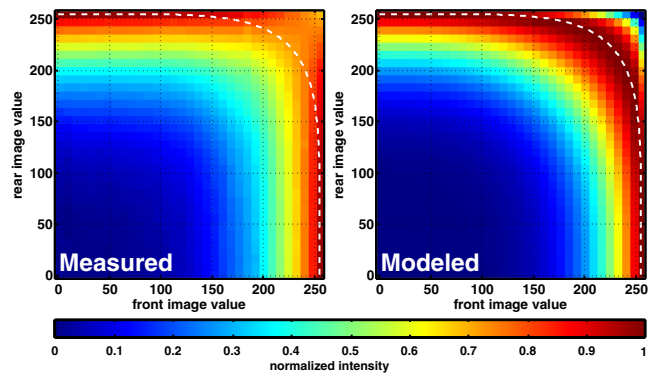

Figure 8: *Radiometric calibration of the prototype. The measured (left) and modeled (right) normalized intensity I is plotted as image values v_1 and v_2 are displayed on the rear and front layer, respectively. The model is a least-squares fit of Equation 11 to the measured intensities. Note that the prototype only uses rotations corresponding to values located on the lower left of the white lines.*

fresh rates of up to 24 frames per second using one iteration for four layers running on the NVIDIA Quadro NVS 450. Figure 4 illustrates SART convergence, demonstrating that 2 to 5 iterations minimize reconstruction artifacts. Estimates for the previous frame may seed the optimization for the current frame. For static scenes, this effectively implements an increasing number of SART iterations over time, while providing a suitable initialization for successive frames in a dynamic environment. Pseudocode and timing trials are included in Supplementary Appendix D.

4.2 Assessment

As shown in Figure 1, polarization fields accurately depict multiple perspectives of the "Buddha" scene. Viewpoint variations capture highlights on the incense burner and occlusions of the background characters. Figure 6 demonstrates faithful reproduction of translucency for the dice and through the windows of the car. Detailed

analysis for each scene is included in Supplementary Appendix B. Smooth motion parallax is shown in the supplementary video.

While confirming the prototype achieves automultiscopic display, photographs exhibit artifacts not predicted by simulations. Moiré is present, although it could be mitigated using the method of Bell et al. [2008]. We attribute intensity artifacts, visible in Figure 6, to discrepancies between the prototype and the ideal construction using polarization-rotating layers. As analyzed in Appendix A and Supplementary Appendix C, the primary discrepancy is the presence of multiple liquid crystal domains in our panels. Furthermore, as characterized by Yeh and Gu [2009], commercial panels do not operate precisely as two-dimensional polarization rotators, particularly at oblique angles. To this end, we used photometric measurements to assess our model. As shown in Figure 8, a photometer measured the normalized intensity I as differing image values v_1 and v_2 were displayed on the rear and front layer, respectively. Substituting Equation 10 into Equation 5 yields the following prediction.

$$I(v_1, v_2) = \sin^2\left\{\sin^{-1}\left[\left(\frac{v_1}{255}\right)^{\frac{\gamma}{2}}\right] + \sin^{-1}\left[\left(\frac{v_2}{255}\right)^{\frac{\gamma}{2}}\right]\right\} \quad (11)$$

Measured intensities are nearly identical upon interchanging v_1 and v_2, validating the additive model in Equation 4—upon which our tomographic optimization relies. Measured contrast is limited when v_1 and v_2 are large. This is confirmed in the supplemental video; overlaying a pair of white images produces a darker image, but with reduced contrast. Thus, artifacts persist in the prototype due to differences between our off-the-shelf panels and ideal polarization rotators. Additional measurements are summarized in Figure 11.

In Figure 7, polarization fields perform comparably to attenuation layers in terms of reconstruction fidelity. Yet, halo artifacts are noticeably reduced. We attribute this primarily to different biases introduced by least-squares optimization of transformed objective functions. As proposed by Gotoda [2010] and Wetzstein et al. [2011], attenuation-based displays optimize an objective, reminiscent of Equation 7, defined for the logarithm of the target intensities. This penalizes artifacts in dark regions, leading to the observed halos. By comparison, polarization fields optimize an objective defined for target intensities transformed by Equation 3; this transformation is more linear than for attenuation, thereby mitigating halos. This is confirmed by the average peak signal-to-noise ratio (PSNR) plots shown in Figure 9, in which polarization fields slightly outperform attenuation layers. Based on these trials, we conclude that polarization fields present an optically-efficient alternative to attenuation layers optimally-suited to multi-layer LCDs, closely mirroring the PSNR trends and dependence on the layer numbers and display thickness previously established for attenuation-based displays.
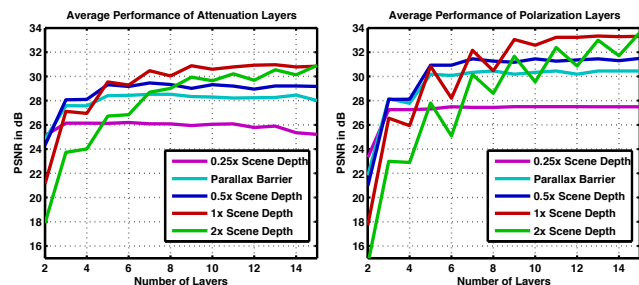

Figure 9: *Average PSNR for attenuation layers vs. polarization fields. The PSNR was averaged for the four scenes in Figure 6 (and for two more in the video) depending on the number of layers and the relative display thickness. Note that polarization fields can accurately present objects beyond the display, but can also be operated in a volumetric mode enclosing the scene for reduced errors.*
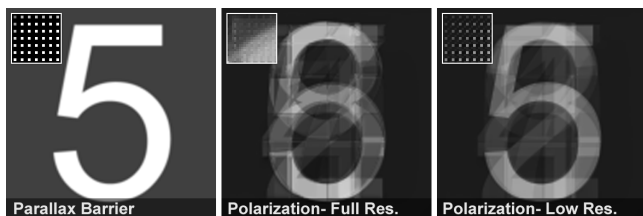

Figure 10: *Uncorrelated views with light field displays. (Left) Parallax barriers allow independent images to be projected in each direction, here corresponding to different Arabic numerals. (Middle) Similar to attenuation layers, polarization fields exploit correlated imagery and significant crosstalk is produced otherwise. (Right) Unlike attenuation layers, constraining only the subset of pixels used by a similar parallax barrier does not resolve this limitation.*

5 Discussion

5.1 Benefits and Limitations

The benefits and limitations of polarization fields were previously outlined in Section 1.2. Here we briefly highlight additional insights drawn from the prototype. Polarization fields have several notable benefits over existing automultiscopic displays, particularly those supporting relatively thin form factors. Foremost, polarization fields are shown to compare favorable to closely-related attenuation layers. Yet, certain practical advantages are afforded by this construction, including increased optical efficiency and reduced reconstruction artifacts. Both methods significantly improve upon the dominant commercial alternatives, being parallax barriers and integral imaging, presenting imagery with greater spatial resolution, increased brightness, and extended depth of field.

Polarization fields inherit many of the limitations of other multi-layer displays. Foremost, performance improves by adding layers and increasing the display thickness, raising costs while restricting the scope for mobile applications. Layered constructions must introduce additional elements to mitigate moiré, scattering, and reflections. By relying on the polarization properties of LCDs, polarization fields require detailed optical models or, alternatively, engineering to produce two-dimensional polarization rotators. Perhaps most significantly, polarization fields converge to a moderate PSNR, even with the benefit of many layers and a large display enclosure. This indicates that such layered constructions have limited degrees of freedom. To this end, Figure 10 considers the performance for light fields for which neighboring views are independent. In contrast to parallax barriers and integral imaging, such imagery is not accurately rendered using polarization fields; thus, such displays share a key limitation with attenuation layers: requiring correlated views such as those that originate from natural scenes.

5.2 Future Work

Additional engineering efforts are required to address prototype limitations. First, our implementation only simulates field sequential color; construction of a strobed LED backlight combined with high-speed monochrome LCDs would be necessary for dynamic color imagery. Second, laboratory measurement of the Jones matrices characterizing the display panels [Moreno et al. 2003; Ma et al. 2010], together with a modified image formation model, would likely minimize artifacts. Third, inclusion of custom holographic diffusers could mitigate moiré and the addition of Fresnel lenses, as proposed by Gotoda [2011], may extend the depth of field. Finally, the LCD panels can be replaced with displays that behave as polarization rotators or, alternatively, additional optical elements may be added to produce a similar result [Moreno et al. 2007].

Beyond these engineering efforts, several promising theoretical opportunities exist. A frequency-domain analysis of polarization fields, following Zwicker et al. [2006], may yield an analytic depth of field expression. A preliminary analysis, performed by evaluating the Fourier transform of Equation 5, indicates spatio-angular frequencies are produced well beyond the region supported by competing parallax barriers and integral imaging constructions. Given the dependence on correlated imagery and the limited degrees of freedom afforded by increasing layers, such performance assessment may be further supported by considering priors on natural light fields. Alternatively, to expand the degrees of freedom, time-multiplexed, multi-layer decompositions may be possible, although necessitating higher-speed panels and likely requiring alternate methods for real-time optimization.

Perhaps the most intriguing direction of future work is to re-examine the full potential afforded by the multi-valued, periodic target polarization field given by Equation 3. In our implementation we only consider the principal value of this expression, limiting the target polarization field to $\theta(u, a) \in [0, \pi/2]$. If this restriction is lifted, additional degrees of freedom appear accessible; for example, larger rotations can *decrease* the intensity of an emitted ray via application of Malus' law. Similarly, incorporating panels that can apply positive and negative rotations over the full range such that $\phi_k(\xi) \in [-\pi, \pi]$ will likely increase reconstruction fidelity and potentially enable efficient, unconstrained optimization methods.

6   Conclusion

Polarization field displays are designed to maximize the optical and computational performance achieved when using multi-layered LCDs for automultiscopic display. Such displays eschew the long-standing trends of refractive, reflective, and attenuation-based architectures, instead focusing on the novel optical properties exhibited by stacked polarization rotators. In this work we establish the potential of such designs, as well as promising avenues of future research that may more fully exploit their potential. As LCDs have become the dominant spatial light modulator employed in consumer displays, it is our hope that polarization fields will inspire others to investigate their full potential for automultiscopic display.

Acknowledgements

References

AKELEY, K., WATT, S. J., GIRSHICK, A. R., AND BANKS, M. S. 2004. A stereo display prototype with multiple focal distances. *ACM Trans. Graph. 23*, 804–813.

ANDERSEN, A., AND KAK, A. 1984. Simultaneous Algebraic Reconstruction Technique (SART): A superior implementation of the ART algorithm. *Ultrasonic Imaging 6*, 1, 81–94.

BELL, G. P., CRAIG, R., PAXTON, R., WONG, G., AND GALBRAITH, D. 2008. Beyond flat panels: multi-layered displays with real depth. *SID Digest 39*, 1, 352–355.

CHAI, J.-X., TONG, X., CHAN, S.-C., AND SHUM, H.-Y. 2000. Plenoptic sampling. In *ACM SIGGRAPH*, 307–318.

CHEN, C.-H., LIN, F.-C., HSU, Y.-T., HUANG, Y.-P., AND SHIEH, H.-P. D. 2009. A field sequential color LCD based on color fields arrangement for color breakup and flicker reduction. *Display Technology 5*, 1, 34–39.

COLEMAN, T., AND LI, Y. 1996. A reflective newton method for minimizing a quadratic function subject to bounds on some of the variables. *SIAM Journal on Optimization 6*, 4, 1040–1058.

DATE, M., HISAKI, T., TAKADA, H., SUYAMA, S., AND NAKAZAWA, K. 2005. Luminance addition of a stack of multidomain liquid-crystal displays and capability for depth-fused three-dimensional display application. *Applied Optics 44*, 6, 898–905.

DAVIS, J. A., MCNAMARA, D. E., COTTRELL, D. M., AND SONEHARA, T. 2000. Two-dimensional polarization encoding with a phase-only liquid-crystal spatial light modulator. *Applied Optics 39*, 10, 1549–1554.

DODGSON, N. A. 2009. Analysis of the viewing zone of multiview autostereoscopic displays. In *SPIE Stereoscopic Displays and Applications XIII*, 254–265.

FAVALORA, G. E. 2005. Volumetric 3D displays and application infrastructure. *IEEE Computer 38*, 37–44.

GOTODA, H. 2010. A multilayer liquid crystal display for autostereoscopic 3D viewing. In *SPIE Stereoscopic Displays and Applications XXI*, vol. 7524, 1–8.

GOTODA, H. 2011. Reduction of image blurring in an autostereoscopic multilayer liquid crystal display. In *SPIE Stereoscopic Displays and Applications XXII*, vol. 7863, 1–7.

HART, W. M. 1987. The temporal responsiveness of vision. In *Adler's Physiology of the Eye*, R. A. Moses and W. M. Hart, Eds. C.V. Moseby Company.

HECHT, E. 2001. *Optics*. Addison Wesley.

IVES, F. E., 1903. Parallax stereogram and process of making same. U.S. Patent 725,567.

JACOBS, A., ET AL. 2003. 2D/3D switchable displays. *Sharp Technical Journal*, 4, 1–5.

JONES, R. C. 1941. A new calculus for the treatment of optical systems. *J. Opt. Soc. Am. 31*, 7, 488–493.

KACZMARZ, S. 1937. Angenäherte auflösung von systemen linearer gleichungen. *Bull. Acad. Pol. Sci. Lett. A 35*, 335–357.

KAK, A. C., AND SLANEY, M. 2001. *Principles of Computerized Tomographic Imaging*. Society for Industrial Mathematics.

KECK, B., HOFMANN, H., SCHERL, H., KOWARSCHIK, M., AND HORNEGGER, J. 2009. GPU-accelerated SART reconstruction using the CUDA programming environment. In *SPIE*, vol. 7258.

LANMAN, D., HIRSCH, M., KIM, Y., AND RASKAR, R. 2010. Content-adaptive parallax barriers: optimizing dual-layer 3D displays using low-rank light field factorization. *ACM Trans. Graph. 29*, 163:1–163:10.

LEVOY, M., AND HANRAHAN, P. 1996. Light Field Rendering. In *ACM SGGRAPH*, 31–42.

LIPPMANN, G. 1908. Épreuves réversibles donnant la sensation du relief. *Journal of Physics 7*, 4, 821–825.

LOUKIANITSA, A., AND PUTILIN, A. N. 2002. Stereodisplay with neural network image processing. In *SPIE Stereoscopic Displays and Virtual Reality Systems IX*, vol. 4660, 207–211.

MA, B., YAO, B., YE, T., AND LEI, M. 2010. Prediction of optical modulation properties of twisted-nematic liquid-crystal display by improved measurement of Jones matrix. *Applied Physics 107*.

MORENO, I., VELÁSQUEZ, P., FERNÁNDEZ-POUSA, C. R., SÁNCHEZ-LÓPEZ, M. M., AND MATEOS, F. 2003. Jones matrix method for predicting and optimizing the optical modulation properties of a liquid-crystal display. *Applied Physics 94*.

MORENO, I., MARTÍNEZ, J. L., AND DAVIS, J. A. 2007. Two-dimensional polarization rotator using a twisted-nematic liquid-crystal display. *Applied Optics 46*, 6, 881–887.

NAYAR, S., AND ANAND, V. 2007. 3D display using passive optical scatterers. *IEEE Computer Magazine 40*, 7, 54–63.

PUTILIN, A. N., AND LOUKIANITSA, A., 2006. Visualization of three dimensional images and multi aspect imaging. U.S. Patent 6,985,290.

STEWART, R. G., AND ROACH, W. R., 1994. Field-sequential display system utilizing a backlit LCD pixel array and method for forming an image. U.S. Patent 5,337,068.

SULLIVAN, A. 2003. A solid-state multi-planar volumetric display. In *SID Digest*, vol. 32, 207–211.

WETZSTEIN, G., LANMAN, D., HEIDRICH, W., AND RASKAR, R. 2011. Layered 3D: tomographic image synthesis for attenuation-based light field and high dynamic range displays. *ACM Trans. Graph. 30*, 4.

YEH, P., AND GU, C. 2009. *Optics of Liquid Crystal Displays*. John Wiley and Sons.

ZWICKER, M., MATUSIK, W., DURAND, F., AND PFISTER, H. 2006. Antialiasing for automultiscopic 3D displays. In *Eurographics Symposium on Rendering*.

A   Modeling Multi-Layer, Multi-Domain LCDs

Artifacts observed in the prototype are not predicted by the polarization rotator model. We show artifacts can be primarily attributed to the presence of multiple liquid crystal domains in the in-plane switching (IPS) panels used in the prototype. By applying the Jones calculus, we introduce a multi-domain LCD model that accounts for artifacts and provides a formal means to assess model limitations.

As described by Yeh and Gu [2009], the Jones matrix modeling an LCD depends on its architecture. Yet, as described by Date et al. [2005], all LCDs are fundamentally retardation-based and can be approximated as *rotated half-wave plates*, with Jones matrix:

$$\mathbf{J}_{\text{HWP}}(\alpha) = \begin{pmatrix} \cos(2\alpha) & \sin(2\alpha) \\ \sin(2\alpha) & -\cos(2\alpha) \end{pmatrix}, \qquad (12)$$

where α is the liquid crystal director angle. Compared to a true polarization rotator, each LCD acts as a *pseudo-rotator*: reversing the polarization state and doubling the rotation angle. The following expression models the normalized intensity for K-layer compositions of single-domain LCDs enclosed by crossed linear polarizers.

$$I_{\text{HWP-K-1}}(\alpha) = I_0 \left| \begin{pmatrix} 0 & 1 \end{pmatrix} \left(\Pi_{k=1}^{K} \mathbf{J}_{\text{HWP}}(\alpha_{K-k+1}) \right) \begin{pmatrix} 1 \\ 0 \end{pmatrix} \right|^2$$
$$= I_0 \sin^2 \left(\sum_{k=1}^{K} (-1)^{k-1} 2\alpha_k \right) \qquad (13)$$
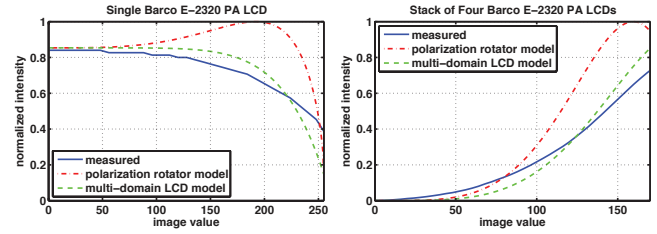

Figure 11: *Radiometric measurements of the prototype. (Left) Normalized intensity for a single panel enclosed by polarizers with a relative rotation of 22.5 degrees. (Right) Normalized intensity for the four-layer prototype (each layer displays the same value). While the multi-domain model is more accurate, the polarization rotator model provides an approximation enabling real-time optimization.*

For the choice $\alpha_k = (-1)^{k-1}\phi_k/2$, this expression is identical to Equation 5. Thus, under this model, multi-layer, single-domain LCDs can approximate layered polarization rotators.

Following Date et al. [2005], we assume every IPS pixel is divided into two domains. Each domain i in layer k is approximated as a rotated half-wave plate $\mathbf{J}_{\text{HWP}}(\alpha_k^{(i)})$ with symmetric directors such that $\alpha_k^{(1)}=-\alpha_k^{(2)}=\alpha$. When the angle between the linear polarizers is not a multiple of 90 degrees, the normalized intensity for a single multi-domain panel differs from Equation 13. In Figure 11, this fact is used to confirm the prototype panels contain multiple domains.

For a multi-layer, multi-domain LCD, rays emitted by the backlight will pass through a single domain in each layer. Considering a bundle of rays passing through a local region, the intensity will depend on the weighted average due to passing through all domain combinations. Summing over combinations yields the following expression for normalized intensity for two-layer, two-domain LCDs.

$$I_{\text{HWP-2-2}}(\alpha) = \frac{I_0}{4} \sum_{i=1}^{2} \sum_{j=1}^{2} \left| \begin{pmatrix} 0 & 1 \end{pmatrix} \mathbf{J}_{\text{HWP}}\left(\alpha_2^{(j)}\right) \mathbf{J}_{\text{HWP}}\left(\alpha_1^{(i)}\right) \begin{pmatrix} 1 \\ 0 \end{pmatrix} \right|^2$$
$$= I_0 \left(\frac{\sin^2(2(\alpha_1 + \alpha_2)) + \sin^2(2(\alpha_1 - \alpha_2))}{2} \right) (14)$$

This expression provides intuition into how multi-layer, multi-domain LCDs deviate from polarization rotators. The first term is proportional to Equation 5, whereas the second term constitutes the error under a polarization rotator approximation. Extending this analysis to four layers yields the following expression.

$$I_{\text{HWP-4-2}}(\alpha) = I_0 \left(\frac{1 - \Pi_{k=1}^{4} \cos(4\alpha_k)}{2} \right) \qquad (15)$$

In Figure 11, we quantify how the polarization rotator approximation deviates from both experiments and the multi-domain model (particularly for large image values). We observe, for small image values or cases for which values are large for a single layer, measurements and the multi-domain model are well approximated.

In conclusion, we identify the presence of multiple domains as the primary source of artifacts. This insight reveals potential solutions. Since the multi-domain model accurately predicts experimental artifacts (see Figure 6), one may consider it as a foundation for an enhanced optimization procedure; however, Equation 15 is non-linear and not directly amenable to real-time optimization via the SART algorithm. Alternatively, replacing panels with single-domain alternatives is predicted, via Equation 13, to better approximate polarization rotators. In practice we expect both strategies must be pursued, together with laboratory characterizations, to obtain the full performance afforded by polarization field displays. Consult Supplementary Appendix C for extended analysis and discussion.